ISSN 1674-1056
http://cpb.iphy.ac.cn
http://iopscience.iop.org/cpb
中国物理 B
Chinese Physics
中国物理
Chinese Physics B

Thermal stability, crystallization, and magnetic properties of FeNiBCuNb alloys

Zhe Chen(陈哲), Qian-Ke Zhu(朱乾科), Shu-Ling Zhang(张树玲), Ke-Wei Zhang(张克维), Yong Jiang(姜勇)

Citation: Chin. Phys. B . 2019, 28(8): 087502. **doi:** 10.1088/1674-1056/28/8/087502
Journal homepage: http://cpb.iphy.ac.cn; http://iopscience.iop.org/cpb

What follows is a list of articles you may be interested in

Grain boundary restructuring and La/Ce/Y application in Nd-Fe-B magnets

Mi Yan(严密), Jiaying Jin(金佳莹), Tianyu Ma(马天宇)

Chin. Phys. B . 2019, 28(7): 077507. **doi:** 10.1088/1674-1056/28/7/077507

Coercivity mechanisms in nanostructured permanent magnets

G P Zhao(赵国平), L Zhao(赵莉), L C Shen(沈来川), J Zou(邹静), L Qiu(邱雷)

Chin. Phys. B . 2019, 28(7): 077505. **doi:** 10.1088/1674-1056/28/7/077505

Regulating element distribution to improve magnetic properties of sintered Nd-Fe-B/Tb-Fe-B composite magnets

Zhu-Bai Li(李柱柏), Jing-Yan Zuo(左敬燕), Dong-Shan Wang(王东山), Fei Liu(刘飞), Xue-Feng Zhang(张雪峰)

Chin. Phys. B . 2019, 28(7): 077503. **doi:** 10.1088/1674-1056/28/7/077503

Micromagnetic simulations of reversal magnetization in cerium-containing magnets

Lei Li(李磊), Shengzhi Dong(董生智), Hongsheng Chen(陈红升), Ruijiao Jiang(姜瑞姣), Dong Li(李栋), Rui Han(韩瑞), Dong Zhou(周栋), Minggang Zhu(朱明刚), Wei Li(李卫), Wei Sun(孙威)

Chin. Phys. B . 2019, 28(3): 037502. **doi:** 10.1088/1674-1056/28/3/037502

Mn-based permanent magnets

Jinbo Yang(杨金波), Wenyun Yang(杨文云), Zhuyin Shao(邵珠印), Dong Liang(梁栋), Hui Zhao(赵辉), Yuanhua Xia(夏元华), Yunbo Yang(杨云波)

Chin. Phys. B . 2018, 27(11): 117503. **doi:** 10.1088/1674-1056/27/11/117503

Thermal stability, crystallization, and magnetic properties of FeNiBCuNb alloys*

Zhe Chen(陈哲)[1], Qian-Ke Zhu(朱乾科)[1], Shu-Ling Zhang(张树玲)[2], Ke-Wei Zhang(张克维)[1,†], and Yong Jiang(姜勇)[1]

[1] School of Materials Science and Engineering, Taiyuan University of Science and Technology, Taiyuan 030024, China
[2] School of Material of Science and Engineering, North Minzu University, Yinchuan 750021, China

(Received 27 March 2019; revised manuscript received 22 May 2019; published online 9 July 2019)

Amorphous $(Fe_{40}Ni_{40}B_{19}Cu_1)_{100-x}Nb_x$ ($x = 1, 3, 5, 7$) ribbons are prepared by using the melt-spinning method. We find that the glass forming ability (GFA) of the as-melt spun ribbons is significantly improved by adding Nb element. In addition, the thermal stability evaluated in steps of $\Delta T = T_{x2} - T_{x1}$ effectively increases from 16 K to 75 K with Nb content increasing. The as-melt spun $(Fe_{40}Ni_{40}B_{19}Cu_1)_{97}Nb_3$ ribbon exhibits a lowest coercivity of 2 A/m and relatively large saturation magnetization of 103.7 A·m^2/kg and thus it can be further treated by being annealed at 809 K. The crystallization behavior is confirmed to be determined by two individual crystallization processes corresponding to the precipitation of $(Fe,Ni)_{23}B_6$ phase and γ-(Fe,Ni) phase. With increasing annealing time, the single $(Fe,Ni)_{23}B_6$ phase can be transformed into a mixture of $(Fe,Ni)_{23}B_6$ and γ-(Fe,Ni) phase, and the grain size of γ-(Fe, Ni) phase increases from 5 nm to 80 nm while the grain size of $(Fe,Ni)_{23}B_6$ remains almost unchanged. Finally, we find that the grain growth in each of $(Fe,Ni)_{23}B_6$ and γ-(Fe, Ni) deteriorates the overall magnetic properties.

Keywords: as-melt spun, glass forming ability, crystallization, coercivity

PACS: 75.50.Kj, 75.47.Np, 75.75.–c, 75.60.Nt **DOI:** 10.1088/1674-1056/28/8/087502

1. Introduction

FeNi based nanocrystalline alloys have shown great potential applications in power electronics due to the advantages of high thermodynamic stability, high glass forming ability (GFA) and good soft magnetic properties.[1–6] In general, nanocrystalline magnetic alloys are obtained by being annealed on magnetic amorphous alloys because proper annealing can relieve the internal stress of the as-melt spun amorphous alloy.[7] Also, after annealing the alloy, the ferromagnetic exchange reaction between soft magnetic nanocrystallites can average out the magnetocrystalline anisotropy and improve the soft magnetic properties if the size and distribution of the nanocrystallites are well controlled.[8–10]

Besides, substitution or addition of insoluble elements such as Cu can act as heterogeneous nucleation sites to facilitate the precipitation of primary crystalline phase. Large atoms such as Nb, Ta, W, and Cr can serve as inhibitors to prevent the grain from growing which is beneficial for improving the soft magnetic properties and glass forming ability (GFA).[11–15] Previous study has suggested that the order of ability to substitute elements in refining grain size of Fe–M–Cu–Si–B alloys is Nb = Ta > Mo = W > V > Cr. Therefore, we select Nb as the additive in this study.[16] On the other hand, the hard magnetic phases like Fe_2B and Fe_3B with high magnetocrystalline anisotropy would provide a great hindrance to the domain wall movement and lead to an increase in coercivity.[17] Therefore, inhibiting the precipitation of hard magnetic phases is also an effective way to improve the soft magnetic properties. It was reported that the coercivity for Fe/Ni = 1 is the lowest due to the hard phase disappearing after being annealed.[1]

In this work, Nb is added into the $Fe_{40}Ni_{40}B_{19}Cu_1$ system, and the effect of Nb content on the thermal stability and the influence of annealing conditions on the crystallization process, microstructures and the magnetic properties of Fe–Ni–B–Cu–Nb alloys are investigated.

2. Experiment

Master alloys with nominal compositions of $(Fe_{40}Ni_{40}B_{19}Cu_1)_{100-x}Nb_x$ ($x = 1, 3, 5, 7$) were prepared by induction melting the mixtures of high-purity elements (Fe:99.99 at.%, Ni:99.99 at.%, B:99.99 at.%, Cu:99.99 at.%, Nb:99.97 at.%,) under an argon atmosphere. The alloys were melted three or four times to achieve homogenization. Then, the master alloys were fabricated in the form of ribbons with about 2 mm in width and 20 μm in thickness, by using a standard procedure of rapid quenching of the melt on a rotating disc (melt-spinning method) with a surface speed of 28.8 m/s. The actual chemical compositions were checked by inductively coupled plasma spectroscopy (ICP) after melt-spinning process. Differential scanning calorimetry (NETZSCH-DSC

*Project supported by the National Natural Science Foundation of China (Grant No. 51731003), the Program for the Top Young Academic Leaders of Higher Learning Institutions of Shanxi Province, China (2014), the "131" Leading Talents Project of Higher Education Institutions in Shanxi Province, China (2015), the Overseas Students Science and Technology Activities Project Merit Funding, China (2016), and the Fund for Shanxi Key Subjects Construction.

†Corresponding author. E-mail: drzkw@126.com

© 2019 Chinese Physical Society and IOP Publishing Ltd

214) measurements were carried out in a stream of helium with a constant heating rate of 15 K/min in a temperature range from room temperature to 923 K. High-temperature microscope (HiTOS-DC) was used to anneal the as-melt spun ribbons at 809 K for different times (10 s, 0.5 min, 1 min, 5 min, 15 min, 30 min). The melt-spun ribbons were annealed by using a rapid thermal process (RTP) in a vacuum below 6×10^{-3} Pa at a heating rate of 200 K/min and argon was introduced as a protective gas to prevent the ribbons from oxidizing.[18,19] The x-ray diffraction (PANalytical X, Pert Power) with Cu $K\alpha$ radiation ($\lambda = 1.5418$ Å) was used to identify the structures of as-melt spun and annealed samples. The magnetization (M_s) and coercivity (H_c) were measured with a vibrating sample magnetometer (VSM, Versalab) and an auto test system of magnetic materials (MATS-2010SD) respectively. The samples for TEM, cut from amorphous ribbons, were thinned after heat treatment by ion beam milling. The transmission electronic microscopy (TEM, JEM 2100F) was performed for the observation of microstructure.

3. Results and discussion

3.1. Effect of Nb-addition on GFA and thermal stability

Figure 1 shows the XRD patterns of the as-melt spun ribbons. It can be seen that the curves for $x = 3$, 5, 7 all exhibit only one broad peak at 45°, indicating that each has a typical FeNi based amorphous structure. For the ribbon with $x = 1$, the XRD curve exhibits a sharp peak together with a broad peak, which suggests partial crystallization in the form of $(Fe,Ni)_{23}B_6$ with the $Cr_{23}C_6$ prototype structure. The Nb is a large radius atom which can enhance the atomic density of the whole alloy, and could result in the enhancement of the stability of the undercooled liquid and suppress the atomic rearrangement for the process of crystallization reaction. It clearly demonstrates that the GFA of the alloys is improved with the addition of Nb. Table 1 shows the actual atomic percentage of the alloy, determined by ICP. The result suggests that the examined composition of the ribbon is close to the nominal composition.

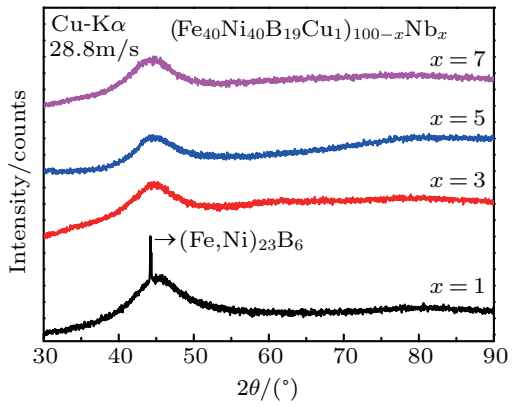


Fig. 1. XRD patterns of $(Fe_{40}Ni_{40}B_{19}Cu_1)_{100}Nb_x$ ($x = 1$, 3, 5, 7) as-melt-spun ribbons.

Table 1. Actual atomic percentage of $(Fe_{40}Ni_{40}B_{19}Cu_1)_{100-x}Nb_x$ ($x = 1$, 3, 5, 7) as-melt spun ribbons.

Nominal compositions	Actual atomic percentage of each element/at.%				
	Fe	Ni	B	Cu	Nb
$(Fe_{40}Ni_{40}B_{19}Cu_1)_{99}Nb_1$	38.49	42.24	17.62	0.99	0.63
$(Fe_{40}Ni_{40}B_{19}Cu_1)_{97}Nb_3$	39.12	40.08	17.15	0.99	2.6
$(Fe_{40}Ni_{40}B_{19}Cu_1)_{95}Nb_5$	37.28	39.88	17.05	1.02	4.7
$(Fe_{40}Ni_{40}B_{19}Cu_1)_{93}Nb_7$	37.31	38.59	16.56	1.00	6.5

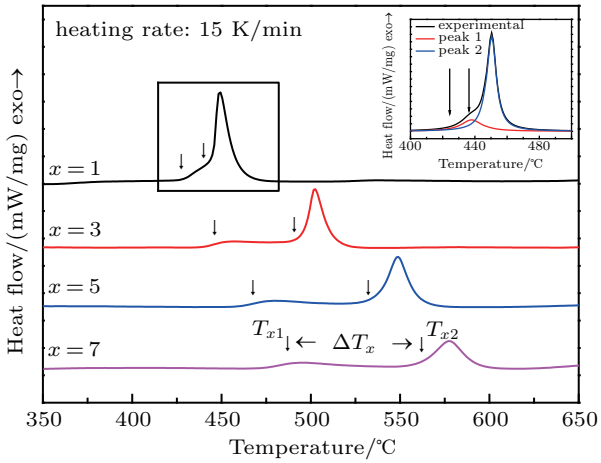


Fig. 2. DSC curves of $(Fe_{40}Ni_{40}B_{19}Cu_1)_{100-x}Nb_x$ ($x = 1, 3, 5, 7$) as-melt spun ribbons.

Figure 2 shows the DSC curves of the as-melt spun ribbons. Two obvious exothermic peaks corresponding to two different crystallization processes can be seen in all the DSC curves. To further determine the crystallization behavior, we select $(Fe_{40}Ni_{40}B_{19}Cu_1)_{97}Nb_3$ ribbons for being pre-annealed at 653 K, 713 K, and 753 K. The XRD results in Fig. 3 show that the $(Fe,Ni)_{23}B_6$ precipitates prior to γ-(Fe, Ni) phase. Therefore, we can determine that the first exothermic peak of DSC, *i.e.*, the sharp peak on the broad peak of $(Fe_{40}Ni_{40}B_{19}Cu_1)_{99}Nb_1$ XRD pattern, is believed to result from the formation of $(Fe, Ni)_{23}B_6$ phase, while the second peak is believed to be due to the formation of γ (Fe, Ni) phase. The first crystallization temperature (T_{x1}) and the second crystallization temperature (T_{x2}) obtained from Fig. 2 are listed in Table 2. Clearly, with the increase of Nb content, T_{x1} increases from 696 K to 754 K and T_{x2} increases from 712 K to 829 K. As a result, the corresponding ΔT increases from 16 K to 75 K, indicating that with the increase of Nb content, the thermal stability of the $(Fe_{40}Ni_{40}B_{19}Cu_1)_{100-x}Nb_x$ ribbons is gradually improved. The effect of Nb element on the onset crystallization temperature of the secondary crystalline phase is stronger than that of the first crystalline phase, which results in the gradual increase of ΔT. Meanwhile, with the increase of Nb content, the exothermic peak width of the secondary crystalline phase increases gradually, indicating that the precipitation process of the γ (Fe, Ni) phase is sensitive to Nb. This may be due to the enhancement of L-S

percolating network structure with the increase of Nb, leading to a higher degree of dense and randomly packed atomic configuration.[20,21] Therefore, the diffusion process of atoms becomes more difficult and further affects the crystallization process.

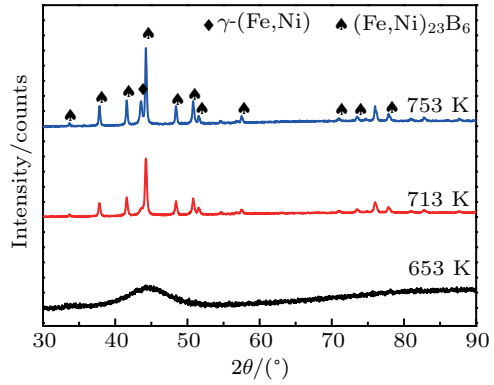


Fig. 3. XRD patterns of as-melt-spun $(Fe_{40}Ni_{40}B_{19}Cu_1)_{97}Nb_3$ ribbons annealed at different temperatures.

Table 2. Thermal stabilities of $(Fe_{40}Ni_{40}B_{19}Cu_1)_{100-x}Nb_x$ ($x = 1, 3, 5, 7$) as-melt spun ribbons

Ribbons	Thermal stabilities		
	T_{x1}/K	T_{x2}/K	$\Delta T = T_{x2} - T_{x1}$/K
$(Fe_{40}Ni_{40}B_{19}Cu_1)_{99}Nb_1$	696	712	16
$(Fe_{40}Ni_{40}B_{19}Cu_1)_{97}Nb_3$	713	760	47
$(Fe_{40}Ni_{40}B_{19}Cu_1)_{95}Nb_5$	736	801	65
$(Fe_{40}Ni_{40}B_{19}Cu_1)_{93}Nb_7$	754	829	75

3.2. Effect of Nb-addition on magnetic property

Figure 4 shows the plots of saturation magnetization (M_s) versus coercivity (H_c) of the as-melt spun ribbons with different Nb content. The specific values of M_s and H_c are summarized in Fig. 5. The lowest H_c of 2 A/m for $x = 3$ is obtained. Moreover, the M_s decreases monotonically from 130.3 A·m^2/kg to 73.7 A·m^2/kg with Nb content increasing from $x = 1$ to $x = 7$. It is well known that the saturation magnetization (M_s) reflects the quantity of total magnetic moment. According to the energy band theory, increasing Nb content means that the concentration of Fe and Ni decrease, thereby leading the total atomic magnetic moment to decrease, and resulting in the decline of M_s. The H_c is known as a structure-sensitive quantity, and it is linked to the internal stress, the relaxation and the local structure. The H_c is relatively high with $x = 1$. The reason may be that the low volume fraction of crystalline phase produced pinning effect hinders the movement of magnetic domains. Table 3 lists the values of H_c and B_s (or M_s) for the $(Fe_{40}Ni_{40}B_{19}Cu_1)_{97}Nb_3$ alloy and some related alloys. Compared with other FeNi magnetic alloys, the as-melt spun ribbon with 3 at.% Nb exhibits excellent soft magnetic properties. It has a relatively low coercivity of 2 A/m and large saturation magnetization of 103.7 A·m^2/kg. Therefore, considering the minimum H_c and relatively high M_s, the ribbon with $x = 3$ is annealed for further research.

Table 3. Values of H_c and B_s (or I_s) of FeNi magnetic alloys.

Materials	H_c/(A/m)	B_s/T or I_s/(A·m2/kg)	References
$Fe_{40}Ni_{38}Mo_4B_{18}$	31.4	.637 T	[22]
$Fe_{40}Ni_{40}P_{14}B_6$	–	87.5 A·m2/kg	[23]
$(Fe_{0.39}Ni_{0.39}B_{0.16}P_{0.06})_{97.5}Nb_{2.5}$	1.0	0.73 T	[24]
$Fe_{42}Ni_{41.7}C_7Si_{4.5}B_{3.9}P_{0.9}$	822.4	88.19 A·m2/kg	[25]
$(Fe_{40}Ni_{40}B_{19}Cu_1)_{97}Nb_3$	2.0	103.7 A·m2/kg≈ 0.935 T	this work

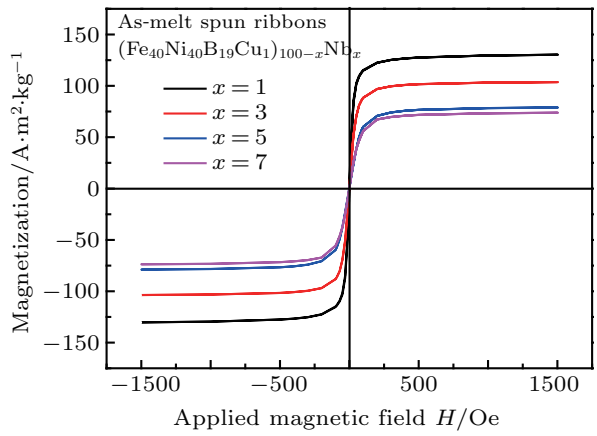


Fig. 4. Saturation magnetization (M_s) *versus* coercivity (H_c) of as-melt spun $(Fe_{40}Ni_{40}B_{19}Cu_1)_{100-x}Nb_x$ ($x = 1, 3, 5, 7$) ribbons.

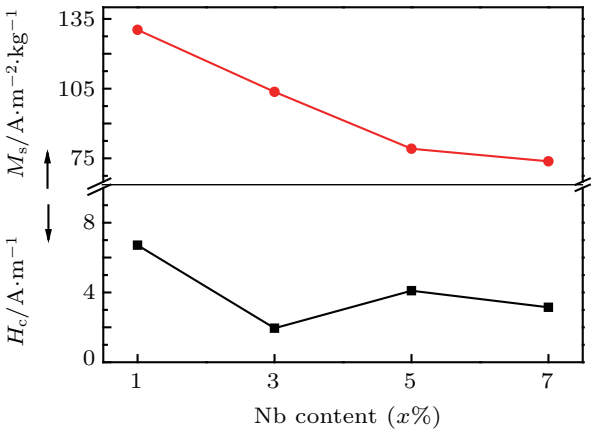


Fig. 5. Saturation magnetization (M_s) and coercivity (H_c) *versus* Nb content for $(Fe_{40}Ni_{40}B_{19}Cu_1)_{100-x}Nb_x$ ($x = 1, 3, 5, 7$) alloy.

3.3. Effect of annealing on crystallization process and magnetic properties

Figure 6 shows the XRD patterns of the $(Fe_{40}Ni_{40}B_{19}Cu_1)_{97}Nb_3$ ribbons annealed at 809 K for different times. It is found that the primary phase is $(Fe,Ni)_{23}B_6$ which precipitates in a very short annealing time of 10 s, followed by the occurrence of FCC γ (Fe, Ni) phase at 0.5 min and then further growing with annealing time increasing. Firstly, the atomic radius of Fe is similar to that of Ni, so that there is a competitive relationship between the formation of γ (Fe, Ni) phase and that of α-Fe phase in the annealing process. On the other hand, the thermal stability of α-Fe phase at high temperature is lower than that of γ (Fe, Ni) phase, so that γ (Fe, Ni) phase prefers to precipitate from an amorphous matrix.[26,27] In contrast, the enthalpy as well as the stability of $(Fe,Ni)_{23}B_6$ phase increases with high Ni content increasing. The short annealing time for the formation of $(Fe,Ni)_{23}B_6$ phase is probably attributed to its instantaneous crystallization process without substantial rearrangement of constituent atoms over longer distance.[28] On the other hand, due to the non-solubility of B in γ-(Fe, Ni) phase, the residual amorphous phase surrounding γ (Fe, Ni) is enriched with B increasing and forms a barrier inhibiting γ (Fe, Ni) phase for further growth, leading to a longer crystallization time than the (Fe, Ni)$_{23}$B$_6$ phase.[14,29]

The values of crystallization activation energy E_1 ($(Fe,Ni)_{23}B_6$) and E_2 (γ-(Fe, Ni)) for the first 2 exothermic peaks of $(Fe_{40}Ni_{40}B_{19}Cu_1)_{97}Nb_3$ ribbons are calculated by both Kissinger equation and Ozava equation and the results are listed in Table 4. Clearly, the value of E_2 is larger than that of E_1, which further confirms the time required for the precipitation of γ-(Fe, Ni) phase is longer than that of the $(Fe,Ni)_{23}B_6$ phase.

Table 4. Crystallization activation energy of as-melt-spun $(Fe_{40}Ni_{40}B_{19}Cu_1)_{97}Nb_3$ ribbons.

Method	E_1/kJ·mol^{-1}	E_2/kJ·mol^{-1}
Kissinger	259.67	437.65
Ozava	258.38	428.39

In order to further investigate the effect of grain size on soft magnetic properties, the average grain size of (Fe, Ni)$_{23}$B$_6$ phase and γ (Fe, Ni) phase for the $(Fe_{40}Ni_{40}B_{19}Cu_1)_{97}Nb_3$ ribbons are estimated by using Scherrer's equation and the results are shown in Fig. 7. It can be seen that the grain size of (Fe, Ni)$_{23}$B$_6$ increases from 33 nm to 38 nm with annealing time increasing from 10 s to 0.5 min and then remains almost unchanged with further annealing while the grain size for γ (Fe, Ni) keeps increasing from 10 nm to 80 nm as annealing time rises, indicating the precipitation of γ (Fe, Ni) can restrain the growth of (Fe, Ni)$_{23}$B$_6$, which is confirmed by the corresponding peak intensity in the XRD patterns in Fig. 6.

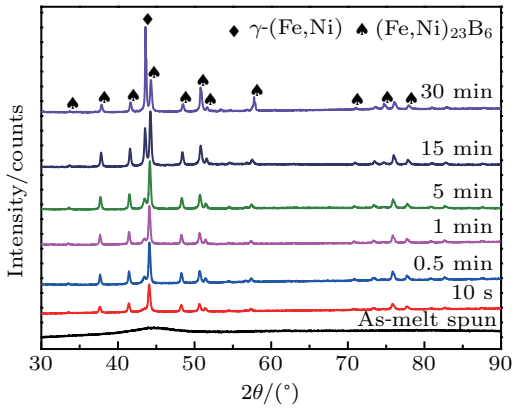


Fig. 6. XRD patterns of as-melt-spun $(Fe_{40}Ni_{40}B_{19}Cu_1)_{97}Nb_3$ ribbons annealed at 809 K for different times.

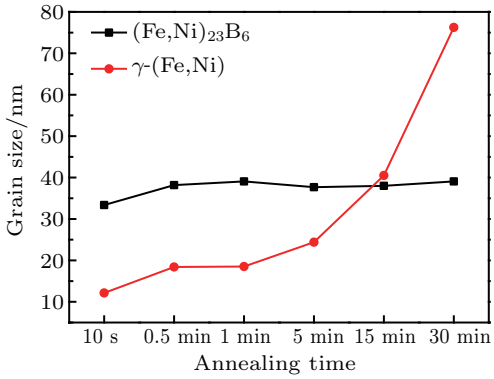


Fig. 7. Dependence of grain size of (Fe, Ni)$_{23}$B$_6$ and γ-(Fe, Ni) on annealing time in $(Fe_{40}Ni_{40}B_{19}Cu_1)_{97}Nb_3$ ribbon at 809 K.

Figure 8 shows the changes of H_c and H_s with annealing time for the $(Fe_{40}Ni_{40}B_{19}Cu_1)_{97}Nb_3$ ribbon. It is found that as the annealing time increases, H_c exhibits an obvious upward trend and eventually reaches to $\sim$ 42.2 A/m. As indicated in the results of Hernando model, soft magnetic properties depend strongly on the nature of the nanocrystal + amorphous+nanocrystal coupling. The increase of H_c after annealing the ribbon for 1 min is attributed to weak intergranular exchange due to the fact that amorphous phases are converted into (Fe, Ni)$_{23}$B$_6$ and γ-(Fe, Ni), while the internal stress has not yet been completely released. When the annealing time increases to 15 min, the internal stress σ disappears, which leads to a slight decrease in H_c.[30,31] However, the gradual growth of (Fe, Ni)$_{23}$B$_6$ and γ-(Fe, Ni) grains cause H_c to rise, thus deteriorating the soft magnetic properties. Compared with other FeNi-based alloys,[32–34] despite lacking α-Fe phase due to the low stability of α -Fe phase in high Ni content FeNi-based alloys, the ribbon still exhibits a relatively low coercivity due to the absence of hard magnetic phases Fe$_2$B and Fe$_3$B. Moreover, M_s is low in the early stage of annealing, which is due to the low volume fraction of γ-(Fe, Ni) phase. However, with further annealing, both (Fe, Ni)$_{23}$B$_6$ phase and γ-(Fe, Ni) phase are precipitated from the amorphous phase, leading to the increase of M_s and then remaining nearly constant at 100 A·m^2/kg after being annealed

for 0.5 min. As M_s is an insensitive parameter, its value is independent of size, distribution and morphology of grains, so M_s maintains a stable value.

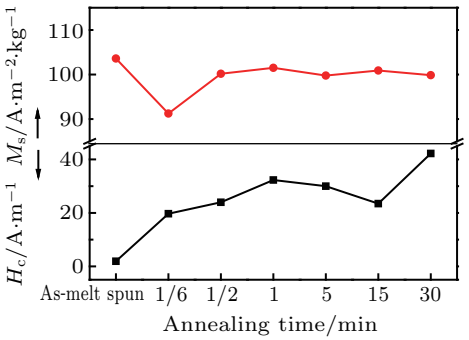


Fig. 8. Dependence of H_c and M_s on annealing time for $(Fe_{40}Ni_{40}B_{19}Cu_1)_{97}Nb_3$ ribbon at 809 K.

Figure 9 shows the high resolution transmission electron micrograph and selected area electron diffraction (SAED) pattern of the as-melt spun $(Fe_{40}Ni_{40}B_{19}Cu_1)_{97}Nb_3$ ribbon. Clearly, the homogeneous amorphous structure is consistent with the XRD pattern. The TEM image in Fig. 10(a) shows that the ribbon is nearly full of nano grains ($\sim$ 40 nm on average) in contact with each other with a little amorphous phase, which is consistent with the XRD patterns as shown in Fig. 6. In such a case, the ferromagnetic exchange reaction is greatly enhanced which explains that the coercivity remains at a relative low value though there are no ferromagnetic nanocrystallites like α-Fe. Moreover, the three diffraction rings corresponding to the crystalline structures of (Fe, Ni)$_{23}$B$_6$ are indexed by planes (422) and (531), and γ-(Fe, Ni) phase is indexed by plane (111). In addition, the detailed analysis of the interplanar fringes of the nanograins confirms the fcc-FeNi structure with the (111) spacing of 0.208 nm in Fig. 10(b) and (Fe, Ni)$_{23}$B$_6$ with the (420) spacing of 0.235 nm in Fig. 10(c).

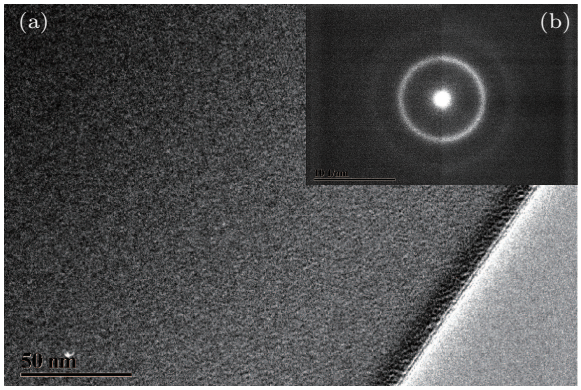


Fig. 9. (a) TEM bright field image and (b) SAED pattern for as-melt-spun $(Fe_{40}Ni_{40}B_{19}Cu_1)_{97}Nb_3$ ribbon.

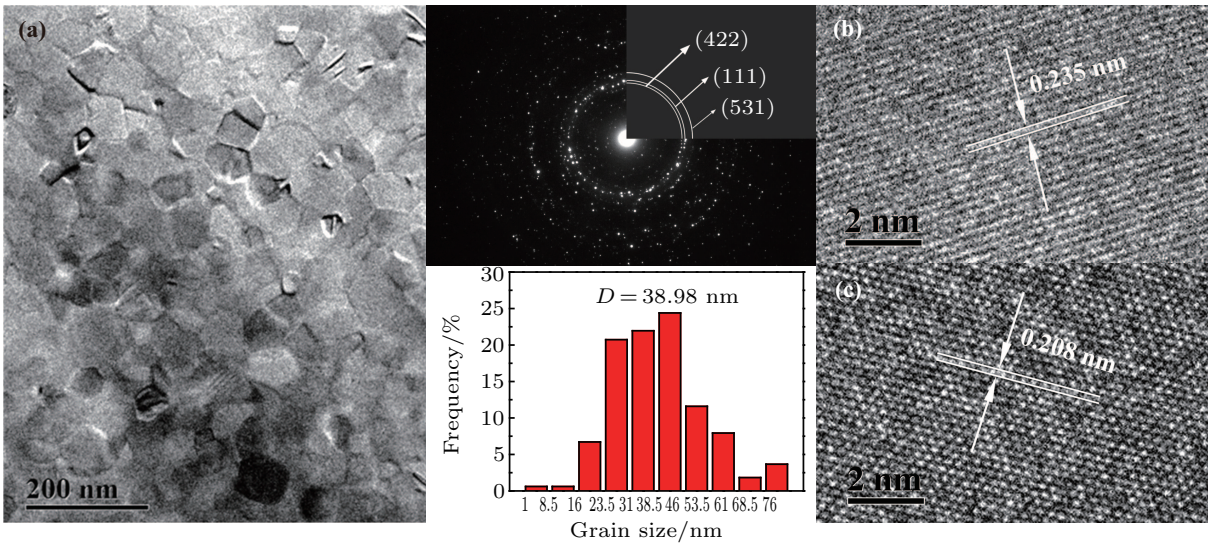


Fig. 10. (a) TEM bright field images, SAED patterns, and grain size distribution for $(Fe_{40}Ni_{40}B_{19}Cu_1)_{97}Nb_3$ ribbon after being annealed at 809 K for 0.5 min. (b) and (c) HREM of $(Fe_{40}Ni_{40}B_{19}Cu_1)_{97}Nb_3$ ribbon after being annealed at 809 K for 0.5 min with marking different interplanar spacing values.

4. Conclusions

In this work, we investigate the effects of Nb addition on glass forming ability and thermal stability of as-melt spun $(Fe_{40}Ni_{40}B_{19}Cu_1)_{100-x}Nb_x$ ($x = 1, 3, 5, 7$) ribbons, and the effect of annealing time on the magnetic properties of the $(Fe_{40}Ni_{40}B_{19}Cu_1)_{97}Nb_3$ ribbon. Several conclusions are drawn below.

(i) With the addition of Nb element, the GFA and thermal stability of $(Fe_{40}Ni_{40}B_{19}Cu_1)_{100-x}Nb_x$ ($x = 1, 3, 5, 7$) ribbons are greatly improved.

(ii) The as-melt spun ribbon with 3 at.% Nb exhibits a lowest coercivity of 2 A/m and relatively large saturation magnetization of 103.7 A·m^2/kg.

(iii) (Fe,Ni)$_{23}$B$_6$ phase is first precipitated in the $(Fe_{40}Ni_{40}B_{19}Cu_1)_{97}Nb_3$ ribbon when annealed at 809 K for 10 s followed by the formation and growth of γ-(Fe, Ni) phase with the longer annealing time.

(iv) With the further increase of annealing time, the

growth of $(Fe,Ni)_{23}B_6$ grain and γ-(Fe, Ni) grain degrades the overall magnetic properties.

References

[1] Vlasak G, Svec P, Kuzminski M, Slawska-Waniewska A, Butvinova B, Butvina P and Hosko J 2011 *J. Alloys Compd.* **509** S64

[2] Milica M Vasić Vladimir A Blagojević Nebojša N and Begović 2015 *Thermochim Acta* **614** 129

[3] Minić D G, Blagojević V A, Mihajlović L E, Cosović V R and Minic´D M 2011 *Thermochim Acta* **519** 83

[4] Tavoosi M and Barahimi A 2017 *Surfaces & Interfaces* **8** 103

[5] Gutiérrez J, Barandiarán J M, MíNguez P, Kaczkowski Z, Ruuskanen P, Vlasák G and Svec P andDuhaj P 2003 *Sensor Actuat A-phys.* **106** 69

[6] Tsepelev V, Starodubtsev Y, Konashkov V and Belozerov V 2017 *J. Alloys Compd.* **707** 210

[7] Kim C W, Cho K H and Suk H G 2014 *Phys. Met. Metallogr.* **115** 1338

[8] Herzer G 1989 *IEEE T Magn.* **25** 3327

[9] Suzki K and Cadogan J M 1998 *Phys. Rev. B* **58** 2730

[10] Herzer G 1990 *IEEE T Magn.* **26** 1397

[11] Long Z L, Chang C T, Ding Y H, Shao Y, Zhang P, Shen B L and Inoue A 2008 *J. Non-Cryst. Solids* **354** 4609

[12] Inoue A and Shen B L 2002 *Mater. T. Jim.* **43** 766

[13] Chang C T, Shen B L and Inoue A 2006 *Appl. Phys. Lett.* **88** 011901

[14] Inoue A, Shen B L and Chang C T 2004 *Acta Mater.* **52** 4093

[15] Kong F, Shen B, Makino A and Inoue A 2011 *Thin Solid Films* **519** 8280

[16] Lu W, Fan J, Wang Y and Yan B 2010 *J. Magn. Magn. Mater.* **322** 2935

[17] Yan Z J, Bian B R, Hu Y, Dang S E, Xia L T and Wang Y M 2010 *J. Magn. Magn. Mater.* **322** 3359

[18] Wang H, Ng S M, Wong H F, Wong W C, Lam K K, Liu Y K, Fei L F, Zhou Y B, Mak C L, Wang Y and Leung C W 2018 *Vacuum* **152** 239

[19] Galesic I, Reusch U, Angelkort C, Lewalter H, Berendes A, Schweda E and Kolbesen B O 2001 *Vacuum* **61** 479

[20] Wu Y, Hui X D, Lu Z P, Liu Z Y, Liang L and Chen G L 2009 *J. Alloys Compd.* **467** 187

[21] Poon S J, Shiflet G J, Guo F Q, Ponnambalam and V 2003 *J. Non-Cryst. Solids.* **317** 1

[22] He K Y, Zhao Y H, Li G G, Cheng L Z, Wu B, Sui M L and Chen W Z 2007 *J. Magn. Magn. Mater.* **316** 34

[23] Ling Z, Ma X H, Li Q, Zhang J J, Dong Y Q and Chang C T 2014 *J. Alloys Compd.* **608** 79

[24] Wang A D, Zhang M G, Zhang J H, Men H, Shen B L, Pang S J and Zhang T 2012 *J. Alloys Compd.* **536** S354

[25] Hwang J Y, Lee H S and Yi S H 2018 *Met. Mater.-Int.* **25** p. 1

[26] Agudo P and Vazquez M 2005 *J. Appl. Phys.* **97** 6044

[27] Elbaile L, Crespo R D, Pierna A R and García J A 2008 *J. Non-Cryst. Solids* **354** 5143

[28] Švec, P, Turčanová J, Janičkovič D, Škorvánek I and Švec Sr P 2009 *The* 13*th International Conference on Rapidly Quenched and Metastable Materials*, 24–29 August, 2008 Dresden, Germany, 012092

[29] Glezer A M, Gorshenkov M V, Zhukov D G, Korchuganova O A, Aleev.A A, Torben Boll, Shurygina N A and Shchetinin I V 2015 *Mater. Lett.* **160** 339

[30] Hernando A, Vázquez M, Kulik T and Prados C 1995 *J. Phys-Condens Matter* **51** 3581

[31] Hernando A, Navarro I I and Gorría P 1995 *J. Phys-Condens Matter* **51** 3281

[32] Saiseng S, Winotai P and Nilpairuch S 2004 *J. Magn. Magn. Mater.* **278** 172

[33] Liu Y J and Chang I T H 2002 *Mater. Sci. Eng. A* **325** 25

[34] Sui M L, Qian L H and He K Y 2000 *Mater. Sci. Eng. A* **286** 201